science.sciencemag.org/content/367/6479/791/suppl/DC1

Supplementary Materials for

Major role of particle fragmentation in regulating biological sequestration of CO_2 by the oceans

Nathan Briggs*, Giorgio Dall'Olmo, Hervé Claustre

*Corresponding author. Email: natebriggs@gmail.com

Published 14 February 2020, *Science* **367**, 791 (2020)
DOI: 10.1126/science.aay1790

This PDF file includes:

Materials and Methods
Figs. S1 to S13
Tables S1 and S2
References

Materials and Methods

Float dataset

All data presented in this study were collected by autonomous profiling floats carrying sensors for chlorophyll a fluorescence (*F*) and particulate optical backscattering (b_{bp}). All data are publicly available in near-real-time as part of the Biogeochemical Argo program. However, the data used here represent a small fraction of the total Biogeochemical Argo dataset, due to the particular requirements of our analyses. The calculations presented below of large-particle concentration, depth attenuation, and especially bulk sinking velocity require measurements of a pulse of large sinking particles that are statistically distinguishable from the background particle concentration at multiple depths in the mesopelagic. In practice, these large particles are rare relative to the volume sampled by the sensor, and high vertical resolution (~1 m or higher) measurements are required in order to obtain useful, depth-resolved concentrations from a single profile. In addition, typical sinking velocities (50-100 m d^{-1}) require temporal frequencies of <5 d in order to sample a sinking pulse multiple times in the upper mesopelagic, where concentrations are more likely to be high enough to constrain sinking velocity measurements. Most Biogeochemical-Argo floats deployed to date profile at 5-10 d intervals and with ≥10 m resolution in the mesopelagic. For this reason, we limited our analysis to data from PROVOR floats whose sampling resolution we modified specifically for resolving pulses of large, sinking particles. These floats permit dynamic control of key sampling parameters. For the purpose of this study, we actively monitored all PROVOR floats deployed in the North Atlantic subpolar gyre and Southern Ocean between 2013 and 2018 and, during each spring/summer phytoplankton bloom we increased their vertical resolution from 10 m to 1 m and temporal resolution from 5-10 d to 2-3 d. High resolution was maintained until we visually confirmed that any associated sinking particle pulse had reached 1000 m. Starting in 2014 we extended high-resolution data at least one month after each pulse in order to better constrain sinking velocities. Excluding obvious sensor failures and/or biofouling, we obtained 110 spring/summer seasons of data from 48 PROVOR floats in the North Atlantic and Southern Ocean during the study period. From these, we visually identified 34 clear, brief pulses of large particles (see signal partitioning in next section) that reached the lower mesopelagic (>500 m). These 34 pulses were used for the fragmentation estimates in this study. These pulses (see Fig. 1 of main text and Table S2) cover primarily the subpolar North Atlantic and the Indian sector of the Southern Ocean north of 52° S during the years 2013-2017. Our quantitative fragmentation results therefore apply primarily to these regions, although we might expect to find similar results in other high-latitude open-ocean blooms. The raw data for these floats can be obtained from the Argo Global Data Assembly Centers in Brest France (ftp://ftp.ifremer.fr/ifremer/argo/dac/coriolis) and Monterey, California (ftp://usgodae.org/pub/outgoing/argo/dac/coriolis) in subfolders named corresponding to the WMO numbers of individual floats given in Table S2. We have also separately published the intermediate (binned) data products from the 34 pulses used in this study along with many of the data processing visualizations presented below, but repeated for all 34 plumes (*26*).

Partitioning of b_{bp} and *F*

We measured Chlorophyll *a* fluorescence *F* and the volume scattering function (at ~124° and 700 nm wavelength) using factory-calibrated WET Labs ECO sensors. These sensors also measured dissolved organic matter fluorescence (FDOM), used here only to aid data quality control (see below). The volume scattering function was converted to the particulate backscattering coefficient b_{bp} by subtracting an estimate of the scattering due to seawater (*27*) and multiplying by $2\pi\chi$, where χ=1.077 (*28*).

We partitioned b_{bp} into three components (see Fig. S1):

$$b_{bp} = b_{bl} + b_{bs} + b_{br}, \tag{1}$$

where b_{bl} is the optical backscattering coefficient due to "large" particles, b_{bs} is the optical backscattering coefficient due to small, labile particles, and b_{br} is a deep blank that includes small refractory particles (see Table S1 for a list of abbreviations). The fraction b_{bl} was separated from b_{bsr} (the sum of b_{bs} and b_{br}; see Fig. S1, red line) by applying an 11-point running minimum filter followed by an 11-point running maximum filter (*21*) to vertical b_{bp} profiles (see Fig. S1 insets, yellow lines). This filter removes positive spikes due to large individual particles that are rare relative to the sample volume of ~10 ml (taking into account ~10 cm of movement during the sensors' 1 s integration time). The residual "spikes" (difference between unfiltered and filtered data) represent b_{bl} plus a background of instrument noise. We quantified this instrument noise component for each sensor by averaging all residual spikes below 300 m from each profile into 50 m vertical bins, pooling all bins from each float and, removing all bins higher than twice the median, and then calculating the median a second time. This instrument noise component can be thought of as a "blank" for our spike signal, and should not be included in our b_{bl} estimate. We therefore added this median blank to the filtered profiles to estimate b_{bsr} (Fig. S1; red line). We then calculated b_{bl} as the difference between total b_{bp} (Fig. S1; black line) and b_{bsr}. The minimum, mean, and maximum b_{bp} "spike blanks" across all sensors were 0.023, 0.039, and 0.062 km^{-1} (note the different units), implying that spikes smaller than this level cannot be distinguished from instrument noise and therefore do not contribute to b_{bl} (but instead contribute to b_{bs}) Assuming a backscattering efficiency of 0.024 and a motion-corrected sample volume of 10 ml, these thresholds correspond very roughly to diameters of 98, 128, and 160 µm (*29*). Then, for each period of interest (~1 month surrounding a large-particle pulse), we estimated b_{br} as the 25th percentile of b_{bsr} from 850-900 m (Fig. S1; blue line). Assuming that b_{br} is constant in both depth and time over our period of interest, we subtracted b_{br} from b_{bsr} to obtain b_{bs}, the backscattering due to small, labile particles (Fig. S1; pink shaded region). The same method was used to partition F into F_l, F_s, and F_r (Fig. S1, right panel). F_l spike blanks ranged from 0.006 to 0.012 mg Chl m^{-3}, roughly equivalent to particle chlorophyll contents of 55-124 pg Chl, given the 10 ml sample volume. Thus, our b_{bl} and F_l signals, although uncalibrated, are estimated for reference to roughly correspond to particles with diameter >100 µm and chlorophyll content >60 pg, respectively, while our b_{bs} and F_s signals correspond to scattering or fluorescence by particles <100 µm in diameter or containing <60 pg Chl. Note that both b_{br} and F_r include any error in factory dark calibration as well as any signal from refractory material. These refractory pools are treated as blanks and not used further in this study, but for reference mean b_{br} and F_r (± standard deviation) for the spring/summer bloom periods analyzed were $(1.9\pm0.6)\times10^{-4}$ m^{-1} and 0.02±0.02 mg m^{-3}, respectively.

Occasionally, we observed very large spikes in b_{bp} ($b_{bl} > 0.008$ m^{-1}) and/or spikes in FDOM measured by the same ECO sensor. Again, assuming backscattering efficiency of 0.024 (*29*), $b_{bl} > 0.008$ m^{-1} corresponds approximately to a diameter of >2 mm. These spikes occurred primarily in discrete layers near 300 m at noon and near the surface at midnight, strongly suggesting that they are caused by live zooplankton or small nekton that are capable of diel vertical migration. We therefore removed all b_{bp} data from within 25 m of such spikes from the analysis. FDOM spikes were identified by subtracting an 11-point median filter to isolate the high-frequency signal. These spikes were identified as high-frequency values exceeding twice the difference between the 10th and 90th percentile for each float. Note that the removal of the largest b_{bl} spikes could potentially cause an under-estimate of sinking particle concentration (and flux) by excluding the very largest (and potentially fastest) sinking particles. If some of these particles fragment into b_{bl} or b_{bs}, they could introduce bias in our fragmentation calculations. We therefore test the impact of removing very large b_{bp} spikes on our results in the sections below and find negligible impact for this dataset.

Processing of large-particle signals

We refer to the method for estimating the fragmentation rates presented in the main text as Method 1A. Unless stated otherwise, all methods described in this and the following sections refer to Method 1A. To estimate large-particle concentrations as well as large-particle loss and fragmentation rates, b_{bl} and F_l were processed via a series of steps detailed in this subsection. We first used large-particle signals b_{bl} and F_l to identify pulses of sinking matter and calculate the associated bulk sinking speeds, w_{bbl} and w_{Fl}. We then binned and smoothed b_{bl} and F_l and calculated their loss rates with respect to depth and time.

We identified 34 pulses of backscattering spikes (b_{bl}) and/or F spikes (F_l) associated with spring or summer blooms in the North Atlantic and Southern Ocean (e.g. Fig. S2, or Fig. 2 of the main text; full list in Table 2). To determine when particle flux peaked at each depth, we visually defined the rough temporal boundaries of each event (e.g. Fig. S2; vertical gray lines) and fit a Gaussian function (at 50 m intervals above 250 m, and 100 m intervals below 250 m due to lower particle concentration) to each large-particle timeseries within these boundaries and below the mixed layer (Fig. S2, black circles and horizontal lines). The width (standard deviation) of the Gaussian function was constrained between 3.5 and 14 days for F_l fits and between 7 and 14 days for b_{bl} fits, and the least-squared fit was optimized using the trust-region method. The center of the sinking pulse within the mesopelagic was then determined using a linear regression (Fig. S2, diagonal black line) between the midpoint depths (independent variable) and the timing of the maximum of each Gaussian fit (dependent variable; see Fig. S2, black circles), weighted by the inverse square of its 95% confidence interval (see Fig. S2, horizontal black lines). Overall, slopes (inverse sinking velocities) ranged from -2 to 3.7 d m^{-1}. Note that negative slopes are not physically meaningful, but can result from uncertainty in the fit. Removing only negative fits could introduce a bias in our calculation of mean slope. To reduce error from poor fits without introducing such bias, we only retained slopes with 95% confidence intervals narrower than ±0.015 d m^{-1}. This filtering reduced the initial 34 pulses to 18 high-precision fits of b_{bl} and 25 of F_l, each spanning multiple regions of both the North Atlantic and Southern Oceans. See Table S2 for individual inverse velocity estimates and regions. The mean slopes (± 2 standard errors) of these high-precision linear regressions across all large-particle pulses are 0.0136±0.0036 d m^{-1} for b_{bl} and 0.0102±0.0025 d m^{-1} for F_l, corresponding to mean sinking velocities (and 95% confidence intervals) of $\overline{w}_{bbl}$ = 74 (58-100) m d^{-1} and $\overline{w}_{Fl}$ = 98 (79-129) m d^{-1}. Given the broad and overlapping confidence intervals, the difference between $\overline{w}_{bbl}$ and $\overline{w}_{Fl}$ is not statistically significant, so it could simply be a result of uncertainty inherent in our calculations. On the other hand, our results may indicate that b_{bl} contains a substantial fraction of detrital aggregates that sink slightly slower than fresh phytoplankton aggregates. Note also that our decision to remove very large b_{bp} spikes (b_{bl} > 0.008 m^{-1}) might remove not only zooplankton (see previous subsection), but also very large, fast-sinking particles, potentially biasing our calculation of $\overline{w}_{bbl}$.

We repeated the above calculations without the very large spike removal step and the difference was minimal: $\overline{w}_{bbl}$ = 78 (59-113) m d^{-1}, indicating that this quality control (QC) step did not substantially bias these results. Separately, we repeated our mean sinking velocity calculations including all 34 plumes for both $\overline{w}_{bbl}$ and $\overline{w}_{Fl}$ and obtained estimates of 74 (57-104) m d^{-1} and 125 (90-206) m d^{-1}, respectively. Again, the impact of this QC step on $\overline{w}_{bbl}$ was minimal. The 28% increase in $\overline{w}_{Fl}$ when the poorest fits are included could indicate moderate low bias in our $\overline{w}_{Fl}$ estimate, but we think it is more likely that the low-quality fits are biased high, since a type-I linear regression on random "noise" should yield a slope of zero (equivalent to infinite sinking speed). In any case, neither of these tests yielded estimates that fell outside of the confidence intervals of our fully QCed estimates. The potential effects of this sinking speed uncertainty on our fragmentation estimates is traced in the error propagation exercise below.

Our calculations of fragmentation rate require estimates of both large-particle concentrations (b_{bl} and F_l) and the net changes in the concentrations of these particles ($\mathrm{d}b_{bl}/\mathrm{d}t$ and $\mathrm{d}F_l/\mathrm{d}t$) as they sink (see Eq. 5). To reliably calculate these derivatives from the noisy large-particle measurements, we binned and smoothed the large-particle data as described below. Large-particle concentrations were first averaged into 6-day, 50-m bins, with so-called Lagrangian, "pulse-following" temporal boundaries centered around each pulse's linear sinking velocity fit (see Fig. S3 for bin edge visualization). The Lagrangian bin boundaries simplify calculation of the net loss rate of large particles. For each pulse, we calculated five temporal bins spanning ±15 days from the maximum of the large-particle pulse and 14 vertical bins spanning from 250 to 950 m. Although floats profiled to 1000 m, the bottom (beginning) 50 meters of each profile were excluded from further analysis because they often contained unrealistically high spikes, which we attribute to material that had accumulated on the top of the float during drift mode. The top 250 m were not used due to higher concentrations of large particles, which can prevent our large/small-particle filter from establishing a baseline free of large particles (*21*). The profiling interval during blooms was usually 2-3 days and occasionally 5 days, so temporal bins of 6 days ensured at least one, usually 2-3 profiles were available per bin. The vertical resolution during surface phytoplankton blooms was 1 m, so at least 50 and usually 100-150 measurements were available per 50 m, 6 d bin, equivalent to 0.5 – 1.5 L, given the 10 ml sample volume. Again, the exclusion of very large b_{bp} spikes could potentially cause a low bias in our b_{bl} estimates, impacting further calculations, so we repeated the bin averaging process with and without the removal of ($b_{bl} > 0.008$ m^{-1}). Inclusion of these data only increased our b_{bl} signals by an average of 1.6%, so the overall impact was negligible. Nevertheless, these occasional spikes did introduce "noise" in a few individual plume calculations, so we still chose to remove them.

To further reduce noise, for Method 1A we smoothed the large-particle data using a so-called "Martin curve" power law (*4*) of the form

$$b_{bl}(z) = b_{bl\_100} * \left(\frac{z}{100}\right)^{-b}, \tag{2}$$

where b represents the strength of the particle attenuation with depth, b_{bl_100} represents b_{bl} at 100 m and the depth z is in meters. An analogous equation was used to smooth F_l as well. Vertical profiles of sinking particle flux below 100 m depth have been repeatedly found to approximate power laws throughout the ocean (*30*), suggesting that this smoothing method can reduce noise in our b_{bl} (and F_l) profiles without introducing substantial biases at any given depth. We verified the appropriateness of the power-law fit for our dataset by averaging binned b_{bl} (and F_l) profiles from all pulses into a single profile and fitting Eq. 2 between 250 and 950 m. These equations fit the mean values within two standard errors at every depth (See Fig. S4), supporting this method of vertical smoothing within the depth bounds of the study. The influence of this smoothing step on our mean fragmentation profile is further explored below alongside other uncertainties (see Method 1B).

To avoid over-fitting Eq. 2, we calculated a single value of b (attenuation of particles with depth) for each 30-day pulse but allowed b_{bl_100} (particle concentration) to vary among the five 6-day temporal bins. The power law exponent b was obtained by averaging all five temporal bins into a single profile (e.g. Fig. S5, colored circles) and optimizing a non-linear least-squares fit of Eq. 2 to the mean b_{bl} (or F_l) profile for the entire 30-day pulse (Fig. S5, black curves). The precision of the fit depends strongly on large-particle concentrations in the shallowest bins. Five of the 34 $b_{bl}(z)$ fits and 11 of the 34 $F_l(z)$ fits yielded very low values at 275 m ($b_{bl} < 4*10^{-5}$ m^{-1} or $F_l < 0.005$ mg m^{-3}) and were excluded from further analysis for Method 1A. Method 1B (see below) included neither the power law smoothing nor this exclusion step. After this step, Method 1A retained fits of both b_{bl}(z) and F_l(z) (e.g. Fig. S5) for 18 pulses, fits of b_{bl}(z) only for 11 pulses, and fits of F_l(z) only for five pulses (see Table S2). For the retained large-particle pulses, b_{bl_100m} and F_{l_100m} were calculated at each temporal bin as the slope of a type-I linear regression, forced through the origin, of dependent variable b_{bl} (or F_l) vs. independent variable $(z/100)^{-b}$ using the fixed value of b determined above. Resultant smoothed profiles for each individual temporal bin (black) are shown together with unsmoothed binned profiles (colors) in Fig. S6.

Depth-resolved estimates of the loss of large-particle concentration with depth (db_{bl}/dz and dF_l/dz) were obtained from the derivative of the "Martin curve" power law with respect to depth. Because the "Lagrangian" temporal bin boundaries were chosen to follow the large-particle population as it sinks, the net loss of large particles with depth can be converted to the net loss rate with respect to time via Eq. 3, where $\overline{w}_{bbl}$ is the mean large-particle sinking speed:

$$\frac{db_{bl}}{dt} = \overline{w}_{bbl} * \frac{db_{bl}}{dz}. \tag{3}$$

Note that due to the Lagrangian frame of reference we adopted, Eq. 3 does not require sink/source terms to account for particles sinking in and out the water parcel under examination. Due to uncertainties in the individual estimates of w_{bbl}, we calculated db_{bl}/dt (and similarly dF_l/dt) for each temporal bin of each bloom using the single mean estimates of $\overline{w}_{bbl}$= 74 m d^{-1} and $\overline{w}_{Fl}$= 98 m d^{-1} calculated earlier in this subsection. Error in mean sinking velocities would lead to systematic bias in db_{bl}/dt and dF_l/dt for all plumes, so sinking velocity was propagated to uncertainty bounds for db_{bl}/dt and dF_l/dt by recalculating Eq. 3 using upper and lower uncertainty bounds of $\overline{w}_{bbl}$ and $\overline{w}_{Fl}$ as input to Eq. 3 (See Table 1). Other sources of uncertainty in db_{bl}/dt and dF_l/dt (e.g. uncertainty in power law fits) were assumed to be random and were not propagated, but contribute to inter-plume variability quantified below. Finally, the smoothed estimates of b_{bl}, db_{bl}/dt, F_l, and dF_l/dt were again averaged into 50 m vertical bins to yield smoothed, binned estimates (Fig. S7).

Processing of small-particle signals

Similar to the large-particle signals, we calculated the net change in small-particle concentration (db_{bs}/dt and dF_s/dt) in a Lagrangian (particle-following) frame of reference, and we calculated mean concentrations and rates of change in the same 6 d, 50 m bins. However, the details of this part of the processing differed for two reasons. First, small-particle concentrations are inherently less noisy than large-particle concentrations (see Fig. S1), so it was not necessary to smooth the data using a power law. Second, small particles sink more slowly, if at all, so their rates of change were calculated between profiles rather than between vertical bins. Small-particle signals were processed as follows.

To define the Lagrangian frame of reference for small particles, we used a range of small-particle sinking speeds $\overline{w}_s$ of 0, 5, and 10 m d-1. Because b_{bs} and F_s include single cells, which are expected to sink at ~1 m d-1 or slower (*31*), the upper limit of 10 m d-1 provides a conservative bound, allowing for a substantial fraction of small particles that sink 10-20 times faster than single cells. Each b_{bs} and F_s profile was first interpolated to a 1 m grid in order to facilitate calculation of the rate of change. Then, for each pair of consecutive float profiles, a profile of $\mathrm{d}b_{bs}/\mathrm{d}t$ was calculated at time t (the midpoint between the two float profiles) as follows

$$\frac{db_{bs}}{dt}(t,z) = \frac{1}{\Delta t}\left(b_{bs}\left(t+\frac{\Delta t}{2}, z+\overline{w}_s\frac{\Delta t}{2}\right) - b_{bs}\left(t-\frac{\Delta t}{2}, z-\overline{w}_s\frac{\Delta t}{2}\right)\right), \tag{4}$$

where Δt is the separation in time between two profiles. We calculated $\mathrm{d}F_s/\mathrm{d}t$ in the same way (replacing b_{bs} with F_s in Eq. 4). In the simplest case of $\overline{w}_s = 0$, Eq. 4 is the difference between two consecutive b_{bs} profiles, divided by Δt. For $\overline{w}_s > 0$, $\mathrm{d}b_{bs}/\mathrm{d}t$ at depth z is calculated using b_{bs} from the previous profile at a shallower "starting" depth than z ($z-\overline{w}_s * \Delta t/2$) and b_{bs} at a deeper "ending" depth than z ($z+\overline{w}_s * \Delta t/2$) from the following profile. Because particle concentrations typically decrease with depth, higher estimates of $\overline{w}_s$ lead to lower (or more negative) estimates of $\mathrm{d}b_{bs}/\mathrm{d}t$. This difference is most important at the top of the mesopelagic, where vertical gradients are the strongest. At each depth, we calculated a central estimate of $\mathrm{d}b_{bs}/\mathrm{d}t$ and $\mathrm{d}F_s/\mathrm{d}t$ based on $\overline{w}_s = 5$ m d-1 and upper and lower bounds based on $\overline{w}_s$ of 10 and 0 m d-1, respectively, for uncertainty propagation. See Fig. S8 for example calculations of $\mathrm{d}b_{bs}/\mathrm{d}t$ and $\mathrm{d}F_s/\mathrm{d}t$. Gridded profiles of both small-particle concentrations (b_{bs} and F_s) and their rates of change ($\mathrm{d}b_{bs}/\mathrm{d}t$ and $\mathrm{d}F_s/\mathrm{d}t$) were averaged in the same 6 d, 50 m bins as the large particles for further processing (see Fig. S9).

Calculation of specific loss rates

This subsection describes the calculation of specific loss rates of optical backscattering fractions b_{bl} and b_{bs}, but applies equally to fluorescence fractions F_l and F_s, substituting b_b with F in all terms and equations below. Assuming no net production of particles in the mesopelagic, we can express $\mathrm{d}b_{bl}/\mathrm{d}t$ as a function of b_{bl} and two specific loss-rate parameters: (1) the large-particle specific consumption rate m_{bbl} that includes ingestion by larger organisms (less egestion) plus remineralization/dissolution by attached organisms, and (2) the specific fragmentation rate D_{bbl} that represents any physical (e.g., shear stress) or biological (e.g., sloppy feeding) processes that break large particles (b_{bl}) into smaller ones (b_{bs}):

$$\frac{db_{bl}}{dt}(z,t) = -\big(m_{bbl}(z,t) + D_{bbl}(\mathrm{z},\mathrm{t})\big)b_{bl}(z,t). \tag{5}$$

Note that D_{bbl} can in principle be negative, indicating net aggregation, for example if small particles stick to a large sinking particle, or if zooplankton consume small particles and produce large fecal pellets. Note also that zooplankton feeding in the surface and producing fecal pellets in the mesopelagic would violate our assumption of no net mesopelagic particle production and introduce a negative bias in our estimate of $\mathrm{d}b_{bl}/\mathrm{d}t$. We further assumed that optical backscattering is conserved when a large particle fragments, so we could express changes in small-particle backscattering db_{bs}/dt as a function of b_{bs}, the small-particle specific consumption rate m_{bbs}, and a source term due to net fragmentation of large particles, $D_{bbl}b_{bl}$:

$$\frac{db_{bs}}{dt}(z,t) = -m_{bbs}(z,t)b_{bs}(z,t) + D_{bbl}(z,t)b_{bl}(z,t). \tag{6}$$

The assumption that fragmentation has minimal effects on bulk optical properties is supported by measurements from both inorganic aggregates in the lab (*29*) and organic aggregates in situ (*21*), showing that *F* remains unchanged and b_{bp} is either unchanged or slightly reduced by fragmentation. These findings are likely due to the low fractal dimension of natural marine aggregates, often below two (*32–34*), which implies that the total particle cross-sectional area concentration (the first-order driver of particulate optical properties) remains constant or even increases with fragmentation. Eqs. 5-6 contain three unknown parameters: m_{bbl}, D_{bbl} and m_{bbs}. In order to estimate all three parameters for each spatiotemporal bin, we introduced an additional term *K*, the ratio of m_{bbl} to m_{bbs}:

$$m_{bbl}(z,t) = m_{bbs}(z,t)K. \tag{7}$$

We assumed that the specific rates of consumption of large particles are greater than or equal to the specific rate of consumption of small particles, because we expect b_{bs} to be either similarly labile to b_{bl} (if freshly produced in the mesopelagic via fragmentation) or perhaps up to 4 times more refractory as “older” b_{bs} may accumulate over the time period of the bloom. Therefore, we bounded *K* between 1 and 4, with a central estimate of 2. The last subsection provides independent estimates of m_{bbs} that independently support the choice of this range.

For each 6 d, 50 m bin, we calculated the three specific loss rates m_{bbs}, m_{bbl}, and D_{bbl} from the five quantities b_{bl}, b_{bs}, db_{bl}/dt, db_{bs}/dt, and *K* by solving Eqs. 5-7. In addition, we calculated the fraction of large-particle loss that is explained by fragmentation as $D^*_{bbl} = D_{bbl}/(D_{bbl} + m_{bbl})$. Fig. S10 shows central estimates of all loss parameters (excluding m_{bbl} and m_{Fl}, which are simply twice m_{bbs} and m_{Fs}, respectively) for all spatiotemporal bins of the example large-particle pulse.

For the uncertainty propagation explained in the next subsection, these calculations were repeated seven times: once using the central estimates of all five quantities, and then six additional times using the upper and lower bounds of db_{bl}/dt, db_{bs}/dt, or *K* along with the central estimates of the other two quantities. These bounds represent potential systematic biases stemming from uncertainty in our estimates of the mean values of $\overline{w}_{bbl}$, $\overline{w}_s$, and *K* (see Table S1).

Mean fragmentation profiles and their uncertainties

Below 500 m and before and after the central particle pulse, F_l was often negligible (see Fig. S7), leading to highly uncertain D_{Fl} fragmentation rates (see Fig. S10). We therefore excluded individual estimates of F_l and F_s loss rates where F_l < 0.005 mg m^{-3} (e.g. Fig. S10, black x’s) from further analysis (Method 1B, below, did not include this exclusion step). We then computed the median profile of each specific loss rate estimate (D_{bbl}, m_{bbl}, m_{bbs}, and D^*_{bbl}, and corresponding *F* loss parameters) across the five temporal bins to obtain a single profile of each specific loss rate for each sinking pulse that reduced the influence of single outliers. Each of these median profiles still contains uncertainty due to several bloom-specific factors, including error in Lagrangian rates of change due to horizontal advection and uncertainty in the power law fits to large-particle concentrations. To obtain a single, more robust estimate across all blooms in all regions of the study, we calculated the mean of all pulse-specific profiles of specific loss rates (see Fig. 3 of main text), and we used two standard errors of this mean as an estimate of its 95% uncertainty bounds due to pulse-specific errors and variability (see Fig. S11, black dashed lines). We re-calculated these median and mean steps using each of the upper and lower bound fragmentation rates due to uncertainty in $\overline{w}_{bbl}$, $\overline{w}_s$, and K. Upper and lower bounds estimates of D and D^* from each individual source of uncertainty are shown in Fig. S11. All uncertainty intervals were added quadratically to calculate combined uncertainty intervals for each estimate (Fig. S11, thin black lines). The largest source of uncertainty in the relative role of fragmentation D^*_{bbl} in the upper mesopelagic was K, the ratio of large- to small-particle specific consumption rate (Fig. S11; red lines). In the lower mesopelagic, $\overline{w}_s$ (Fig. S11; blue lines) and inter-pulse variability (Fig. S11, black dashed lines) dominated D^*_{bbl} uncertainty. Inter-pulse variability was the dominant source of D^*_{Fl} uncertainty at nearly all depths. The large-particle sinking velocity $\overline{w}_l$ was a major source of uncertainty in specific fragmentation rates D_{bbl} and D_{Fl}, but not in the relative role of fragmentation in attenuating flux, because $\overline{w}_l$ affected our estimates of total large-particle flux attenuation and fragmentation in roughly the same proportion.

We also computed regional mean fragmentation profiles for the North Atlantic and Southern Ocean (See Fig. 4 of main text). In this case, we do not present complete uncertainty budgets, but show only two standard errors around the mean (inter-pulse variability), fixing K and w at our global central estimates of K=2, $\overline{w}_{bbl}$ = 74 m d^{-1}, $\overline{w}_{Fl}$ = 98 m d^{-1}, and $\overline{w}_s$ = 5 m d^{-1}. This presentation highlights the statistically significant difference between North Atlantic and Southern Ocean mesopelagic particle dynamics. As long as K and w parameters are indeed constant between hemispheres, this result implies a significant difference in fragmentation rates.

Method 1A (the primary method described above) includes several steps designed to reduce and quantify “noise” in our final mean fragmentation estimates. To address the possibility that these steps introduce bias in our mean profiles of D and D^*, we recalculated D and D^* profiles using a second, simpler methodology: “Method 1B” (Fig. S11, green symbols). We started Method 1B with the same bin-averaged estimates of b_{bl} and F_l as Method 1A, but three processing steps were omitted. First, for Method 1B, b_{bl} and F_l were not smoothed using a power-law fit. Second, blooms with low b_{bl} and F_l in the shallowest bin were not excluded, so that all 34 blooms were included in both D_{bbl} and D_{Fl} calculations. Third, no bins with low values of F_l (Fl<0.005 mg m^{-3}) were excluded. Instead, taking b_b for example, all six-day 50 m bin-averaged estimates of b_{bl} from each depth (n=170, including five temporal bins for each plume) were averaged to obtain a single mean profile of b_{bl}. A single mean d$b_{bl}(z)$/dz profile was estimated as d$b_{bl}(z)$/dz = (b_{bl}(z+50)-b_{bl}(z-50))/100[m] and converted to d$b_{bl}(z)$/dt via Eq. 3, using our central estimate of w_{bbl}. Individual six-day 50 m bin-averaged estimates of b_{bs} and db_{bs}/dz were similarly averaged into single mean profiles for all 34 plumes. Mean D_{bbl} and m_{bbl} profiles were then calculated as in Method 1A by solving Eqs. 5-7, using the same central estimates of K and w_{bbs} (see Table S1). D^*_{bbl} was again calculated as $D_{bbl}/(D_{bbl} + m_{bbl})$. The same Method-1B steps were repeated for F to calculate D_{Fl} and D^*_{Fl}. The resulting Method-1B mean D_{bbl}, D^*_{bbl}, D_{Fl} and D^*_{Fl} profiles (Fig. S11, green symbols) were more variable with depth but did not show clear, systematic differences from the central Method-1A estimates (thick black lines). This result suggests that our first-order Method-1A findings that high, depth-dependent fragmentation rates explain roughly half of mesopelagic flux attenuation are not artifacts of the smoothing or data removal steps designed to improve precision of our final estimates. Our Method 1A and Method-1B mean D^*_{Fl} results did show opposite trends with depth (Fig. S11, lower right panel), suggesting, along with the wide Method-1A confidence intervals, that the apparent increase in

D_{*Fl} with depth is not a robust result, but the overall importance of D_{*Fl} in the mesopelagic was unchanged. In addition, Method-1A D_{bbl} estimates exceeded Method-1B estimates (Fig. S11, upper left) at all depths below 700 m, suggesting that the power-law fit in Method 1A might have caused an over-estimate of all large-particle loss processes in the lower mesopelagic (see Fig. S4 showing that mean large-particle attenuation with depth below 700 m may be over-estimated by a power law). However, the uncertainty in both methods prevent any strong conclusions on this subject.

Alternative estimates of specific loss rates m_{bbs} and m_{Fs}

In order to check the assumptions of Method 1, including the likely range of K and our estimates of w_l, we compared our Method 1 estimates of small-particle specific loss rates m_{bbs} and m_{Fs} (derived from Eqs. 5-7) with estimates from two alternative methods not involving assumptions about either K or w_l: Method 2, using early spring data, and Method 3, again using data from the sinking particle pulses. Mean values for all three results agree within uncertainty bounds (Fig. S12), supporting the validity of our methods and assumptions.

For Method 2, we identified 12 events of early spring mixed-layer shoaling from three floats in the North Atlantic. In each event, rapid mixed-layer shoaling caused a mesopelagic particle population with elevated F_s to become isolated from surface production for ≥ 2 d. For a depth range that did not appear to be influenced by vertical mixing (i.e. low db_{bs}/dz), we calculated $b_{bs}(t)$ as described above and estimated m_{bbs} by least squares fit of $b_{bs}(t)$ to Eq. 8, where t_0 is the time of the first profile following stratification:

$$b_{bs}(t) = b_{bs}(t_0)\exp\big(-m_{bbs}(t - t_0)\big). \tag{8}$$

Eq. 8 is a transformation of Eq. 6, with the fragmentation term removed due to negligible large-particle concentrations in the early spring (confirmed by b_{bl} and F_l measurements). Depth ranges were between 150 and 300 m. An example calculation is shown in Fig. S13. The same process was repeated for small-particle chlorophyll fluorescence (F_s) to estimate its specific loss rate m_{Fs}. Two of the 12 fits of m_{bbs} were rejected because b_{bs} was not significantly > 0. The remaining 10 m_{bbs} estimates and all 12 m_{Fs} estimates were significantly > 0. The mean m_{bbs} and m_{Fs} of all events, plus or minus two standard errors were 0.102±0.028 d^{-1} and 0.180±0.048 d^{-1}, respectively (Fig. S12; thick black lines). While these estimates correspond to a slightly earlier time period than our bloom calculations and contain no Southern Ocean data, they are valuable because they are simpler, involving no assumptions about large particles or fragmentation, so the approximate agreement with our Method 1 m_{bbs} estimates (Fig. S12) at 275 m is reassuring.

For Method 3, we used the same binned estimates of b_{bl} and b_{bs}, and db_{bs}/dt as Method 1 (e.g. Figs. S7 and S9). However, we further assumed that m_{bbs} and D_{bbl} were constant over a 30-day time period (all five temporal bins) and 100 m depth range (two vertical bins). This assumption allowed us to simultaneously solve for m_{bbs} and D_{bbl} using only Eq. 6 and multiple measurements of b_{bl} and b_{bs}, and db_{bs}/dt. Estimates of db_{bl}/dt (which in turn relies on $\overline{w}_{bbl}$) and K were not needed, so that Method 3 provides a check on Method 1 parameterizations of $\overline{w}_{bbl}$ and K. However, the ability to simultaneously constrain m_{bbs} and D_{bbl} via Eq. 6 (without Eq. 5 or Eq. 7) relies on the dynamic range of the time-varying measurements of b_{bs}, b_{bl}, and db_{bs}/dt, so we chose only the six large-particle pulses accompanied by the highest maximum F_s observed between 500-550 m. Pulses that occurred <1 month after deep mixing events (MLD>200 m) were excluded from this analysis to ensure that mesopelagic b_{bs} (and F_s) originated from recent sinking and/or fragmentation, rather than vertical mixing (as in Method 2), in case the specific loss rates of these two particle populations differed.

At 100 m intervals, centered at 200-800 m, Method 3 estimates of m_{bbs} and D_{bbl} were obtained by multiple linear regression, forced through the origin, of $\mathrm{d}b_{bs}/\mathrm{d}t$ as a function of $D_{bbl}b_{bl}$ and $-m_{bbs}b_{bs}$ (see Eq. 6), calculated using our central estimate of small-particle sinking velocity $\overline{w}_s$ = 5 m d^{-1}. Each regression contained ten data points (five temporal bins by two depth bins). The mean m_{bbs} profiles ± 2 standard errors from all six blooms are shown as gray lines in Fig. S12 (left panel). Method 3 was repeated with fluorescence measurements to obtain m_{Fs} as well (Fig. S12, right panel). Method 1 estimates (Fig. S12, bold colored lines) fell within the bounds of Method 3 estimates of m_{bbs} and m_{Fs} (gray lines) at all depths (Fig. S12). While uncertainty bounds are large, these results provide further confidence in Method 1, including our estimates of w_l and our choice of K.

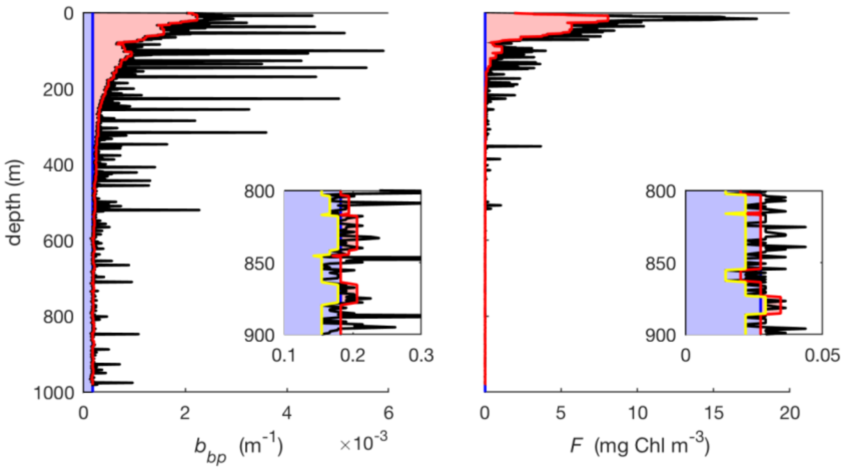

Fig. S1. Example partitioning of b_{bp} and F profiles. Black lines show total b_{bp} (left) or F (right) at native resolution. Yellow lines (insets) show low-pass "spike removal" filters. Red lines show b_{brs} (left) and F_{rs} (right) the sum of refractory and small labile particle signals. The difference between red and yellow lines (insets) represents the deep "spike blank" for this bloom period, or the contribution of sensor noise to the high frequency "spike" signal. The difference between black and red lines is the large-particle signal b_{bl} (left), or F_l (right). Blue lines show deep blanks b_{br} (left; well above zero presumably due to refractory material) and F_r (right; near zero, as refractory pool does not contain chlorophyll) for the bloom period. The difference between red and blue lines (shaded pink) is b_{bs} (left) or F_s (right), the contribution of small, labile particles. Data are from float WMO6901523, June 2013 (Example pulse 1 in main text).

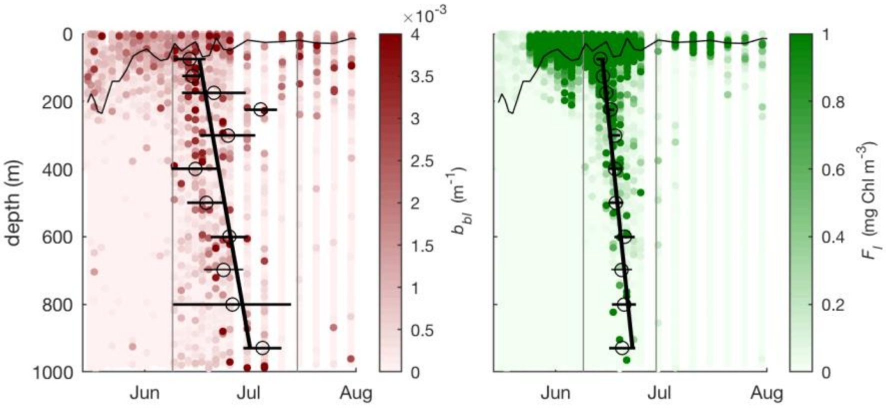

Fig. S2. Example calculation of bulk large-particle sinking velocities. Colored circles show raw large-particle (spike) signals b_{bl} (red) and F_l (green), with higher values (larger spikes) plotted on top of lower values. Single dark circles against lighter background show the optical signals of single particles. The thin black line shows the mixed-layer depth. Vertical gray lines show initial, visual temporal boundaries of large-particle pulse. Open black circles show timing of the maximum of Gaussian fits to large-particle timeseries, and bold horizontal black lines show the 95% confidence interval of this timing. The diagonal bold black lines show the weighted linear fit to these maxima with respect to depth, used to calculate sinking velocities. Data are from float WMO6901523, 2013 (Example pulse 1 in main text).

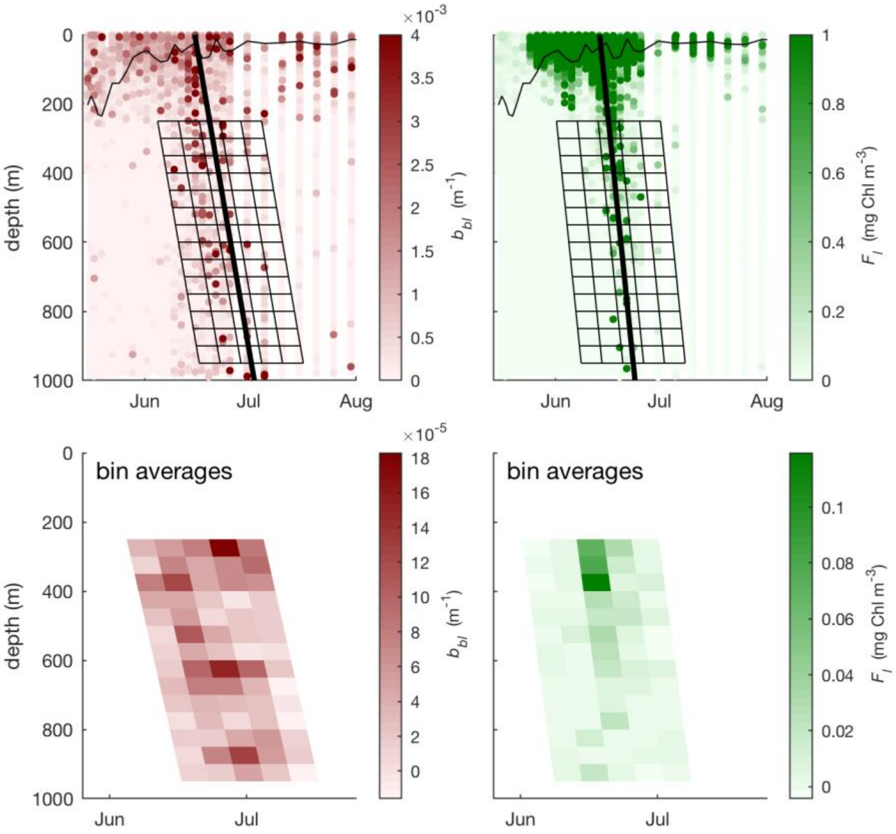

Fig. S3. Bin averaging of large-particle signals. Upper panels show b_{bl} and F_l, as in Fig. S2, but with bin boundaries overlaid (black grid). Lower panels show bin-averaged b_{bl} and F_l. Data are from float WMO6901523, 2013 (Example pulse 1 in main text). A document containing similar plots for all 34 plumes can be found at seanoe.org (*26*).

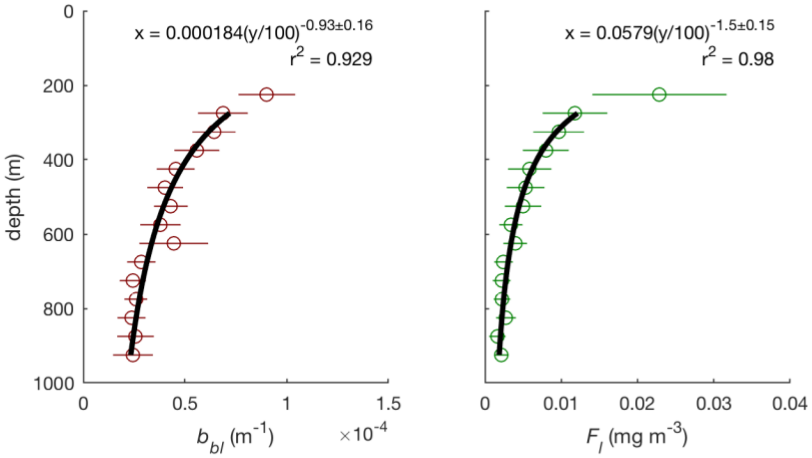

Fig. S4. Mean binned large-particle profiles from all particle plumes. Circles show means of all temporal bins from all 34 pulses, horizontal lines show two standard errors around the mean, and black curves and equations show least-squared power-law fits to the mean profiles.

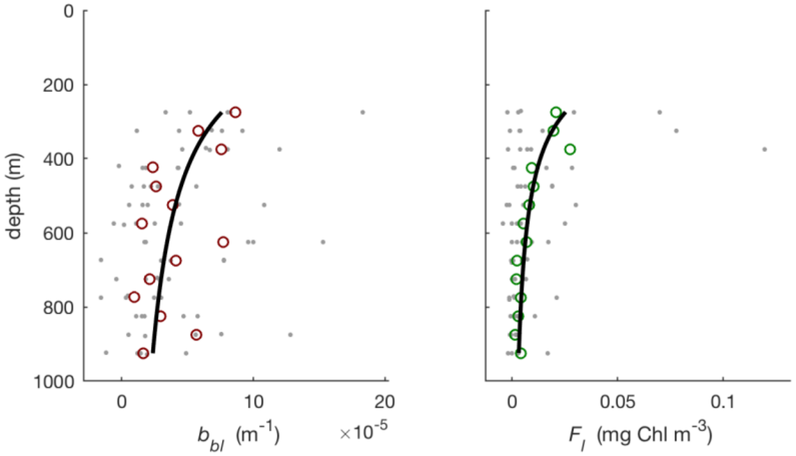

Fig. S5. Example fits of "Martin curve" power laws to smooth large-particle profiles. Gray points show individual 6-day, 50 m bin averages of b_{bl} (left) and F_l (right). Red and green circles show averages of the five temporal bins, and black curves show least-squared power law fits to these average profiles: b_{bl} = 0.000201[m$_{-1}$](z/100)$_{-0.96}$ and F_l = 0.14[mg m$_{-3}$](z/100)$_{-1.7}$. Data are from float WMO6901523, 2013 (Example pulse 1 in main text).

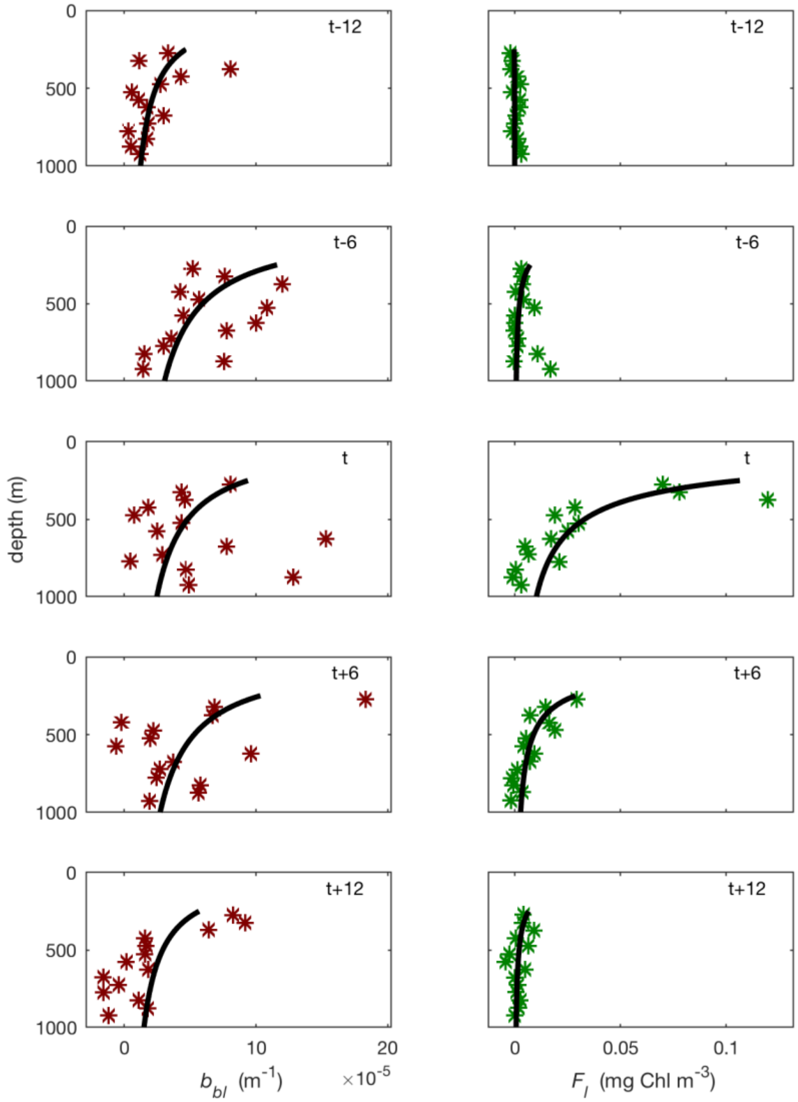

Fig. S6. Smoothing of large-particle signals for each temporal bin. The timing of the temporal bin center, relative to time of pulse maximum (*t*), given above each panel, ranges from *t*-12 (top panels) to *t*+12 (bottom panels). Red and green stars show unsmoothed 6-day, 50 m binned b_{bl} and F_l, respectively. Black curves power-laws (with exponent held constant) fit to each temporal bin. Data are from float WMO6901523, 2013 (Example pulse 1 in main text).

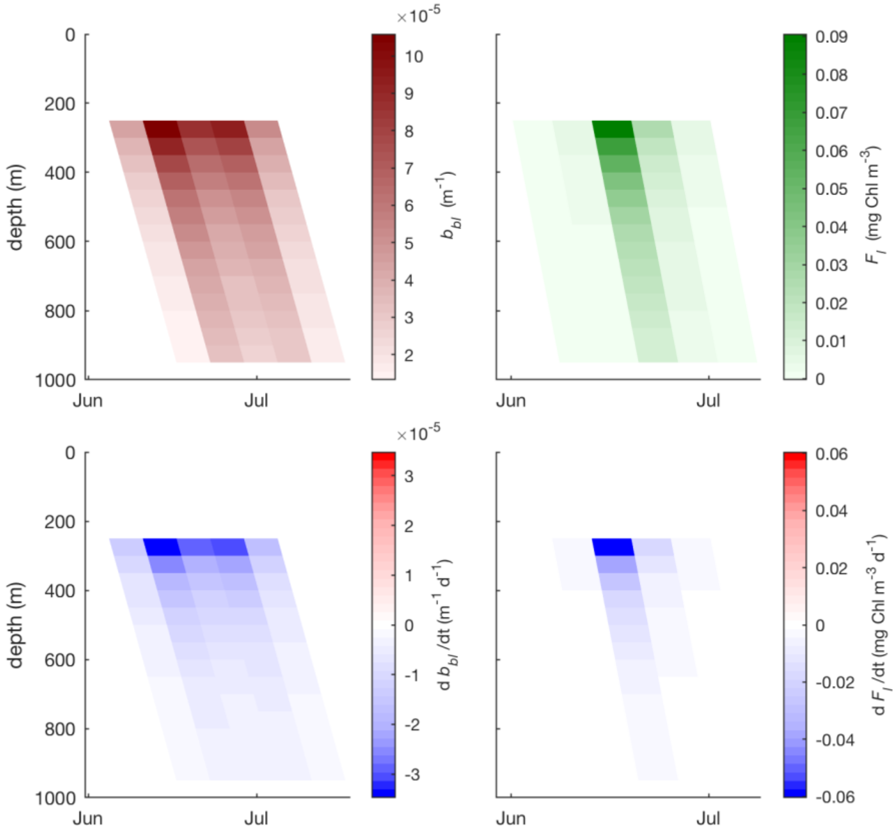

Fig. S7. Smoothed, binned estimates of large-particle concentrations and their specific net loss rates. Data are from float WMO6901523, 2013 (Example pulse 1 in main text). A document containing similar plots for all 34 plumes can be found at seanoe.org (*26*).

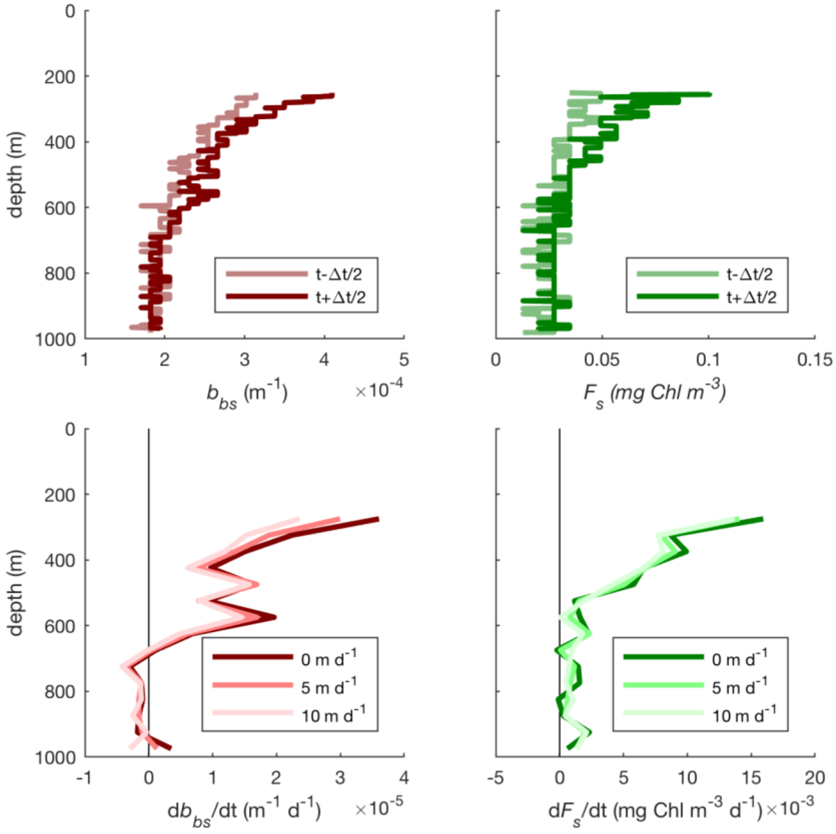

Fig. S8. Calculation of db_{bs}/d*t* and dF_s/d*t*. Top panels show small particle concentrations from two consecutive profiles, with paler colors indicating the earlier profiles. Bottom panels show derived estimates of db_{bs}/d*t* (left) and dF_s/d*t* (right), bin averaged at 50 m intervals, with colors in lower panels indicating different assumed small-particle sinking velocities ($\overline{w}_s$): 0, 5, and 10 m d^{-1} in order of dark to light. Data are from float WMO6901523, June 2013 (Example pulse 1 in main text).

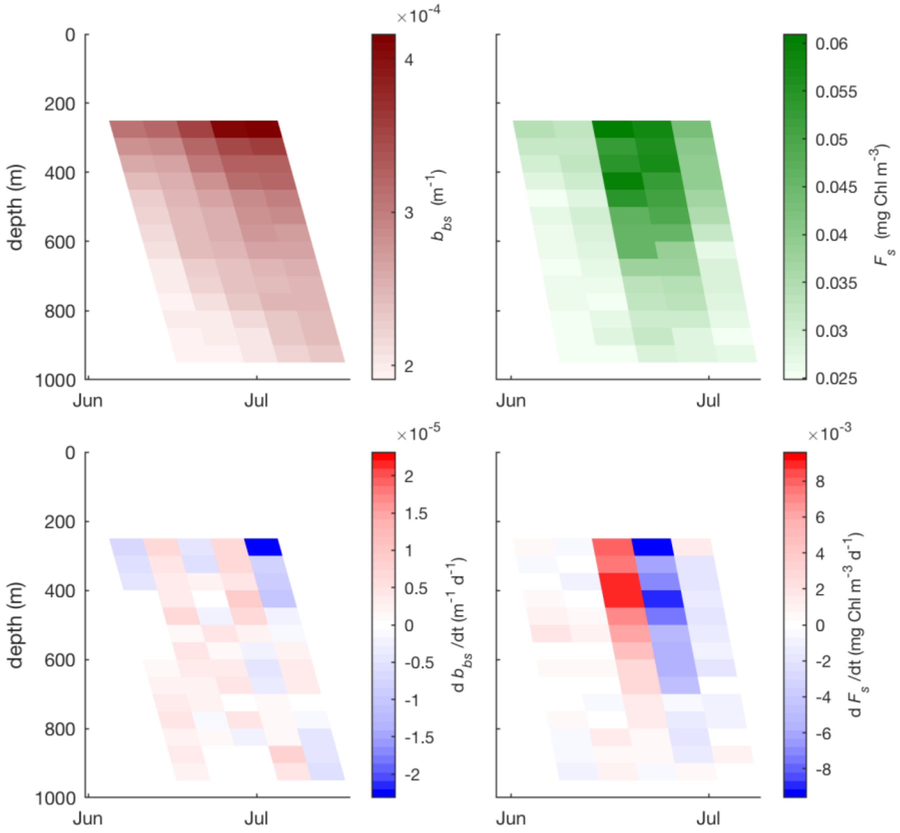

Fig. S9. Bin-averaged small-particle concentrations and their net rates of change. Net rates of change are calculated in a Lagrangian (particle-following) frame of reference, shown here assuming a central estimate of small-particle sinking speed, $\bar{w}_s$ = 5 m d^{-1}. Data are from float WMO6901523, 2013 (Example pulse 1 in main text). A document containing similar plots for all 34 plumes can be found at seanoe.org (*26*).

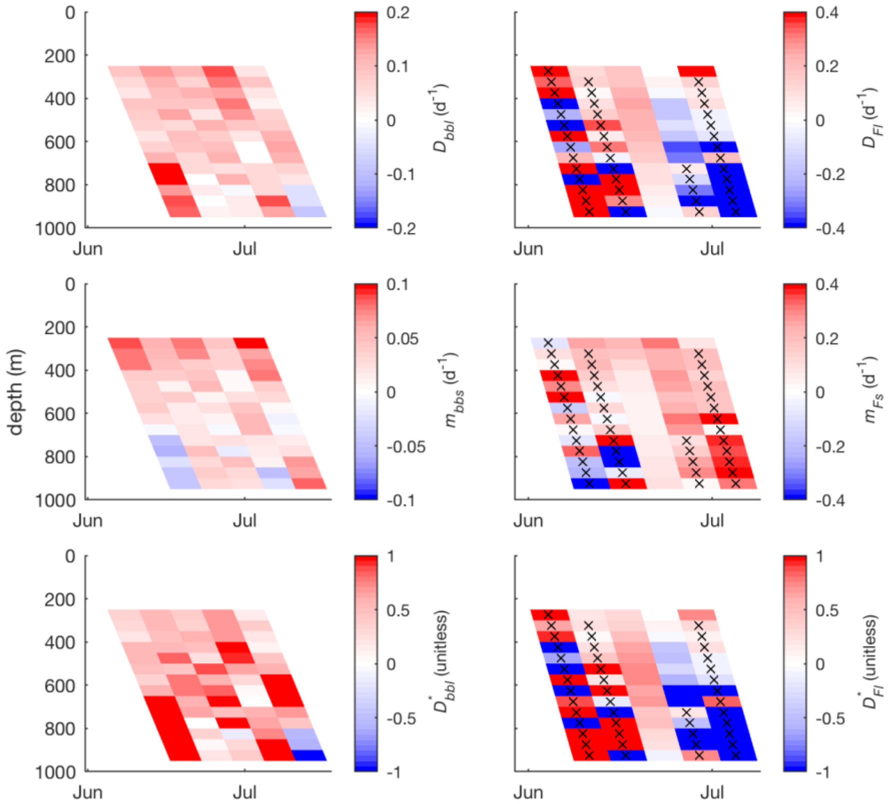

Fig. S10. Central estimates of mesopelagic particle loss terms in 6 d, 50 m bins for example bloom. Black x's show bins that are excluded from analysis due to low F_l. Data are from float WMO6901523, 2013 (Example pulse 1 in main text). A document containing similar plots for all 34 plumes can be found at seanoe.org (*26*).

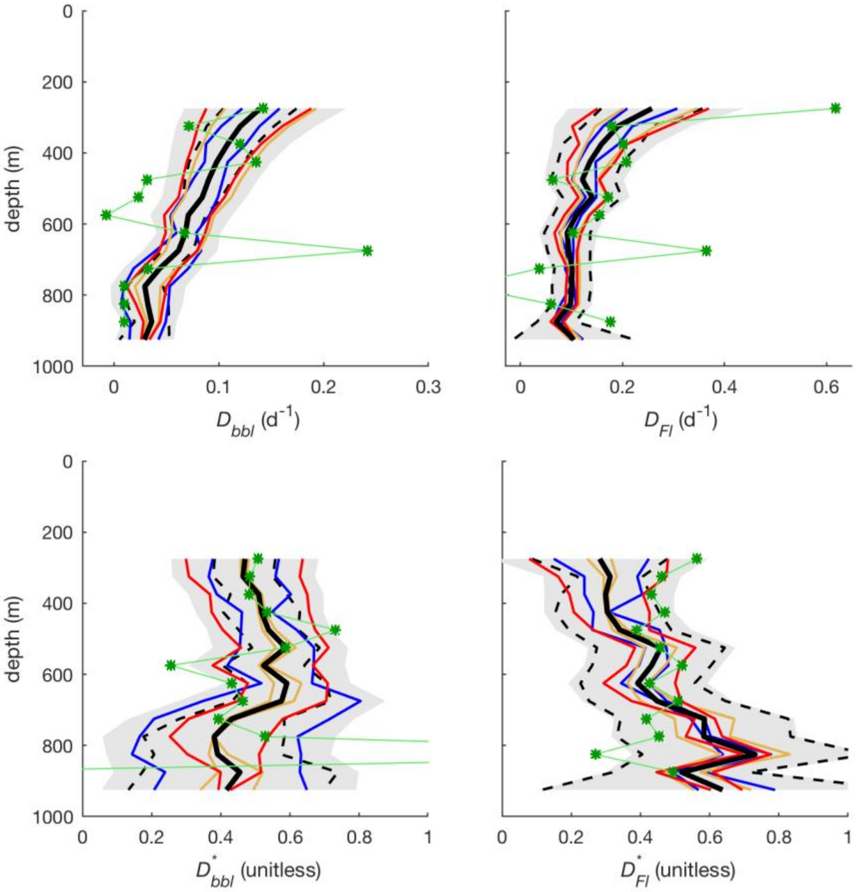

Fig. S11. Uncertainty budgets for mean fragmentation terms. Each panel shows central estimates of mean fragmentation terms across all pulses (thick black lines), along with uncertainty bounds due to pulse-specific error and variability (dashed black lines), mean small-particle sinking velocity $\overline{w}_s$ (blue), mean large-particle sinking velocity $\overline{w}_l$ (orange), and the ratio of large- to small-particle specific consumption rate K (red). The total uncertainty bounds (from the root sum of squares of all individual uncertainty intervals) is shaded in gray. Alternative "Method 1B" central mean fragmentation profiles, calculated without the vertical smoothing step and without removal of low b_{bl} or F_l, are shown in green.

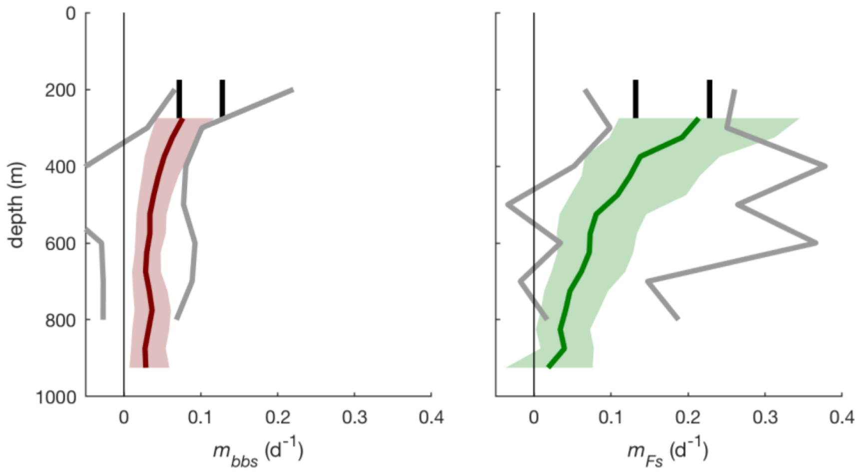

Fig. S12. Alternative calculations of small-particle specific loss rates. Colored lines show the primary estimates (Method 1A), including mean (dark lines) and confidence intervals (light shaded areas). Thick black lines show depth range and confidence intervals of the mean of early-spring estimates (Method 2). Gray lines show confidence intervals of the mean of the alternative bloom-period estimates (Method 3).

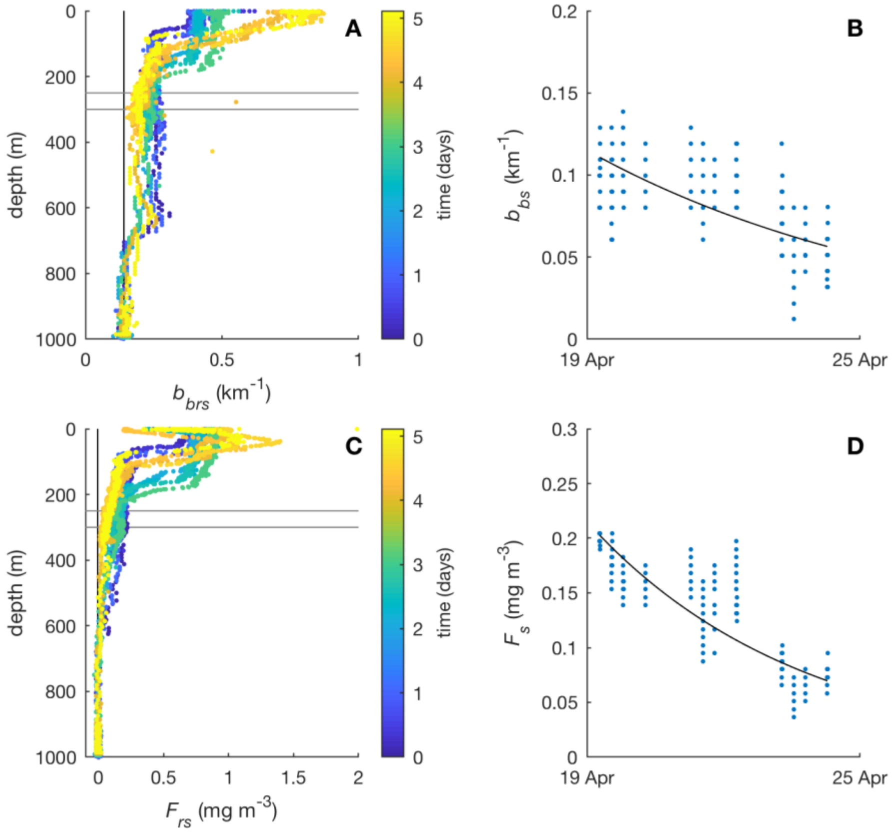

Fig. S13. Example Method-2 calculation of m_{bbs} and m_{Fs}. (A) Vertical profiles of b_{brs} showing progressive loss of a stranded small-particle population between 250 m and 600 m over five days following mixed-layer shoaling. Colors show time in days since the day of the first profile. Vertical black lines show estimates of deep "blank" b_{br}, and horizontal gray lines show depth window of m_{bbs} calculations. (B) Timeseries of b_{bs} in the 250-300 m window (blue) and least-squared fit of exponential Eq. S8 (black curve). (C) Vertical profiles of F_{rs} (colors and lines following panel A). (D) Timeseries of F_s in the 250-300 m window (blue) and least-squared fit of exponential Eq. S8 (black curve). Data in all panels are from float WMO6901647, 2015.

Table S1. Abbreviations used in this manuscript.

Symbol	Central Value (confidence range)†	Units	Description
b_{bl}		m^{-1}	b_{bp} due to large particles
b_{bp}		m^{-1}	particulate optical backscattering coefficient
b_{br}		m^{-1}	b_{bp} due to refractory particles (includes sensor blank)
b_{bs}		m^{-1}	b_{bp} due to small, labile particles
b_{brs}		m^{-1}	$b_{br} + b_{bs}$
D_{bbl}		d^{-1}	specific loss rate of b_{bl} due to fragmentation
D_{bbl*}		–	Fraction of total b_{bl} loss due to fragmentation
D_{Fl}		d^{-1}	specific loss rate of F_l due to fragmentation
D_{Fl*}		–	Fraction of total F_l loss due to fragmentation
F		mg Chl m^{-3}	Chlorophyll *a* fluorescence (factory calibrated)
F_l		mg Chl m^{-3}	F due to large particles
F_r		mg Chl m^{-3}	F due to refractory particles (interpreted as sensor blank)
F_s		mg Chl m^{-3}	F due to small particles
F_{rs}		mg Chl m^{-3}	$F_r + F_s$
K	2 (1-4)	–	Ratio of m_{bbl}/m_{bbs} or m_{Fl}/m_{Fs}
m_{bbs}		d^{-1}	specific loss rate of b_{bs}
m_{bbl}		d^{-1}	specific loss rate of b_{bl} due to direct consumption
m_{Fs}		d^{-1}	specific loss rate of F_s
m_{Fl}		d^{-1}	specific loss rate of F_l due to direct consumption
$\overline{w}_{bbl}$	74 (58-100)	m d^{-1}	mean sinking velocity of large "marine snow" particles
$\overline{w}_{bbs}$	5 (0-10)	m d^{-1}	mean sinking velocity of small, labile particles
$\overline{w}_{Fl}$	98 (79-129)	m d^{-1}	mean sinking velocity of chlorophyll within large particles
$\overline{w}_{Fs}$	5 (0-10)	m d^{-1}	mean sinking velocity of chlorophyll within small particles

†Central Values only given for constant parameters used in fragmentation calculations

Table S2. Overview of large-particle pulses analyzed.

See Table 1 for definition of terms in the column headings. Region abbreviations are for the Iceland Basin (ICB), Irminger Sea (IRS), Labrador Sea (LAS), other North Atlantic (NAT), Crozet Islands (CRO), East of Kerguelen Islands (KER_E), West of Kerguelen Islands (KER_W), and other Southern Ocean (SO). Example pulses (Fig. 2 of main text) are shown in bold font.

Float WMO Number	b_{bl} pulse date	region	LAT (°N)	LON (°E)	w_{bbl}^{-1} (d m^{-1})	w_{Fl}^{-1} (d m^{-1})	b_{bl} power-law exponent	F_l power-law exponent	b_{bl} 275 m (m^{-1})	F_l 275 m (mg m^{-3})	D_{bbl} 275 m (d^{-1})	D_{Fl} 275 m (d^{-1})	D_{bbl}^* 275 m	D_{Fl}^* 275 m
6901516	6-Jun-13	ICB	62.27	-21.96	0.019±0.012	0.012±0.003	-0.69±0.55	-2±1.3	9.10E-05	0.012	0.03	0.28	-0.15	0.33
6901520	30-May-13	ICB	61.54	-24.41	-	0.021±0.013	-0.94±0.6	-	0.00013	0.0037	0.04	-	0.22	-
6901647	3-Jun-15	ICB	59.14	-24.77	0.018±0.013	0.011±0.004	-	-0.33±0.99	3.80E-05	0.0077	-	-0.09	-	-0.30
6901647	8-Jun-17	ICB	63.44	-26.54	0.021±0.012	0.015±0.004	-0.74±0.82	-2.8±0.81	0.00018	0.027	0.06	0.54	0.23	0.52
6901523	1-Jul-14	IRS	60.50	-33.66	0.008±0.01	-	-0.47±0.52	-	0.0001	2.10E-07	0.08	-	0.58	-
6901482	30-Jun-14	IRS	63.29	-33.31	0.008±0.01	-	-0.31±0.67	-	8.70E-05	0.00097	0.06	-	0.47	-
6901519	30-Jun-14	IRS	59.01	-33.19	0.012±0.009	-	-0.24±0.56	-1.8±4.4	8.30E-05	0.0054	0.07	0.37	1.26	0.64
6901523	**15-Jun-13**	**LAS**	**57.44**	**-49.96**	**-**	**0.01±0.003**	**-0.96±0.77**	**-1.7±0.72**	**7.60E-05**	**0.025**	**0.11**	**0.30**	**0.41**	**0.28**
6901527	25-May-15	LAS	58.02	-49.24	0.009±0.006	0.009±0.002	-	-2.2±0.85	2.60E-05	0.028	-	0.53	-	0.67
6901486	22-May-15	LAS	58.47	-50.99	0.021±0.007	0.007±0.004	-	-2.4±0.88	2.10E-05	0.037	-	0.60	-	0.69
6901524	28-May-15	LAS	57.06	-43.18	-	0.01±0.011	-	-3.7±0.52	2.70E-05	0.022	-	0.85	-	0.69
6901527	3-Jul-16	LAS	57.33	-45.00	-	0.006±0.007	-	-1.2±1.4	3.10E-05	0.0092	-	0.19	-	0.37
6901525	14-May-14	NA	48.65	-43.71	0.006±0.008	0.006±0.007	-0.77±0.53	-1±0.51	6.10E-05	0.023	0.14	0.23	0.58	0.29
6901516	16-Jun-14	NA	52.86	-34.83	0.006±0.005	0.005±0.003	-0.27±0.54	-	4.10E-05	0.0022	0.01	-	0.28	-
6901575	10-Nov-15	CRO	-44.06	49.68	-	0.019±0.008	-0.8±0.54	-1.5±0.87	5.30E-05	0.017	0.06	0.12	0.30	0.21
6901493	10-Nov-15	CRO	-44.06	49.65	0.026±0.015	0.016±0.01	-0.99±0.74	-2.1±0.67	6.20E-05	0.017	0.08	0.14	0.33	0.07
6901583	27-Nov-15	CRO	-44.14	53.20	0.017±0.009	0.002±0.003	-0.5±0.52	-0.72±0.84	5.50E-05	0.015	0.07	-0.13	0.33	-0.16
6901578	14-Nov-16	CRO	-45.61	63.61	-	-	-1.2±0.44	-	5.80E-05	0.0049	0.11	-	0.41	-
6901490	5-Feb-15	KER_E	-48.68	72.85	0.004±0.011	0.005±0.003	-1.9±0.69	-1.1±0.67	9.00E-05	0.011	0.34	0.36	0.60	0.64
6901004	5-Feb-15	KER_E	-48.71	72.77	-0.002±0.012	0.005±0.006	-1.7±1.5	-0.9±0.56	9.70E-05	0.0085	0.31	0.24	0.63	0.70
6901583	2-Dec-16	KER_E	-48.98	83.68	0.019±0.012	0.009±0.01	-0.73±0.5	-1.1±1.2	5.90E-05	0.0077	0.08	0.05	0.47	-0.06
6902734	13-Dec-16	KER_E	-49.12	73.39	-	-	-1.3±0.58	-1.6±0.4	8.80E-05	0.033	0.23	0.45	0.57	0.66
6902738	**11-Dec-16**	**KER_E**	**-48.50**	**72.04**	**-**	**0.009±0.007**	**-1.2±0.58**	**-1.3±0.33**	**0.00011**	**0.056**	**0.23**	**0.32**	**0.69**	**0.84**
6902735	8-Dec-16	KER_W	-52.67	68.28	-	0.003±0.009	-0.72±0.71	-	4.60E-05	0.0041	0.11	-	0.55	-
6902739	10-Dec-16	KER_W	-52.75	68.19	-	0.001±0.005	-1.3±0.42	-2.3±0.86	5.80E-05	0.0056	0.20	0.89	0.58	0.40
6901574	11-Jan-16	KER_W	-50.66	67.25	-	0.002±0.011	-2.2±1	-	7.20E-05	0.0031	0.34	-	0.54	-
6901579	13-Feb-15	KER_W	-51.78	67.49	-	-	-1.4±0.91	-	5.60E-05	0.0016	0.27	-	0.72	-
6901574	9-Feb-15	KER_W	-51.80	67.52	-	-	-1.2±0.54	-	6.20E-05	0.0017	0.21	-	0.69	-
6901575	14-Dec-17	SO	-46.64	108.43	-	0.019±0.006	-1.5±0.4	-2±1	9.40E-05	0.0065	0.18	1.55	0.40	0.66
6901583	1-Jan-18	SO	-48.87	116.81	-	0.014±0.014	-1.1±0.82	-	5.10E-05	0.0012	0.14	-	0.41	-
6901578	24-Dec-17	SO	-46.27	95.03	0.019±0.009	0.018±0.007	-1.2±0.53	-4.1±2.2	7.10E-05	0.0076	0.10	0.45	0.33	0.43
6902737	20-Dec-17	SO	-52.17	82.00	0.02±0.015	-	-1.7±0.59	-1.4±0.38	0.00012	0.0065	0.15	0.19	0.31	0.43
6902736	31-Dec-17	SO	-52.46	96.61	-	-	-2.1±1.2	-4.6±1.9	0.00011	0.0055	0.26	0.98	0.47	0.64
6901492	20-Dec-13	SO	-41.96	10.34	0.014±0.014	0.019±0.007	-0.98±0.66	-1.2±1.2	4.80E-05	0.0087	0.12	0.03	0.38	0.40

References and Notes

1. P. W. Boyd, T. W. Trull, Understanding the export of biogenic particles in oceanic waters: Is there consensus? *Prog. Oceanogr.* **72**, 276–312 (2007). doi:10.1016/j.pocean.2006.10.007
2. S. A. Henson, R. Sanders, E. Madsen, P. J. Morris, F. Le Moigne, G. D. Quartly, A reduced estimate of the strength of the ocean's biological carbon pump. *Geophys. Res. Lett.* **38**, L04606 (2011). doi:10.1029/2011GL046735
3. D. A. Siegel, K. O. Buesseler, S. C. Doney, S. F. Sailley, M. J. Behrenfeld, P. W. Boyd, Global assessment of ocean carbon export by combining satellite observations and food-web models. *Global Biogeochem. Cycles* **28**, 181–196 (2014). doi:10.1002/2013GB004743
4. J. H. Martin, G. A. Knauer, D. M. Karl, W. W. Broenkow, VERTEX: carbon cycling in the northeast Pacific. *Deep Sea Res. Part A Oceanogr. Res. Pap.* **34**, 267–285 (1987). doi:10.1016/0198-0149(87)90086-0
5. L. Guidi, L. Legendre, G. Reygondeau, J. Uitz, L. Stemmann, S. A. Henson, A new look at ocean carbon remineralization for estimating deepwater sequestration. *Global Biogeochem. Cycles* **29**, 1044–1059 (2015). doi:10.1002/2014GB005063
6. S. A. Henson, R. Sanders, E. Madsen, Global patterns in efficiency of particulate organic carbon export and transfer to the deep ocean. *Global Biogeochem. Cycles* **26**, GB1028 (2012). doi:10.1029/2011GB004099
7. E. Y. Kwon, F. Primeau, J. L. Sarmiento, The impact of remineralization depth on the air-sea carbon balance. *Nat. Geosci.* **2**, 630–635 (2009). doi:10.1038/ngeo612
8. X. Irigoien, T. A. Klevjer, A. Røstad, U. Martinez, G. Boyra, J. L. Acuña, A. Bode, F. Echevarria, J. I. Gonzalez-Gordillo, S. Hernandez-Leon, S. Agusti, D. L. Aksnes, C. M. Duarte, S. Kaartvedt, Large mesopelagic fishes biomass and trophic efficiency in the open ocean. *Nat. Commun.* **5**, 3271 (2014). doi:10.1038/ncomms4271 Medline
9. M. A. St. John, A. Borja, G. Chust, M. Heath, I. Grigorov, P. Mariani, A. P. Martin, R. S. Santos, A Dark Hole in Our Understanding of Marine Ecosystems and Their Services: Perspectives from the Mesopelagic Community. *Front. Mar. Sci.* **3**, 31 (2016). doi:10.3389/fmars.2016.00031
10. J. R. Collins, B. R. Edwards, K. Thamatrakoln, J. E. Ossolinski, G. R. DiTullio, K. D. Bidle, S. C. Doney, B. A. S. Van Mooy, The multiple fates of sinking particles in the North Atlantic Ocean. *Global Biogeochem. Cycles* **29**, 1471–1494 (2015). doi:10.1002/2014GB005037
11. A. Belcher, M. Iversen, S. Giering, V. Riou, S. A. Henson, L. Berline, L. Guilloux, R. Sanders, Depth-resolved particle-associated microbial respiration in the northeast Atlantic. *Biogeosciences* **13**, 4927–4943 (2016). doi:10.5194/bg-13-4927-2016
12. D. M. Karl, G. A. Knauer, J. H. Martin, Downward flux of particulate organic matter in the ocean: A particle decomposition paradox. *Nature* **332**, 438–441 (1988). doi:10.1038/332438a0

13. S. L. C. Giering, R. Sanders, R. S. Lampitt, T. R. Anderson, C. Tamburini, M. Boutrif, M. V. Zubkov, C. M. Marsay, S. A. Henson, K. Saw, K. Cook, D. J. Mayor, Reconciliation of the carbon budget in the ocean's twilight zone. *Nature* **507**, 480–483 (2014). doi:10.1038/nature13123 Medline

14. G. Dall'Olmo, K. A. Mork, Carbon export by small particles in the Norwegian Sea. *Geophys. Res. Lett.* **41**, 2921–2927 (2014). doi:10.1002/2014GL059244

15. L. R. Pomeroy, D. Deibel, Aggregation of Organic Matter By Pelagic Tunicates. *Limnol. Oceanogr.* **25**, 643–652 (1980). doi:10.4319/lo.1980.25.4.0643

16. B. A. Biddanda, L. R. Pomeroy, Microbial aggregation and degradation of phytoplankton-derived detritus in seawater. I. Microbial succession. *Mar. Ecol. Prog. Ser.* **42**, 79–88 (1988). doi:10.3354/meps042079

17. S. Goldthwait, J. Yen, J. Brown, A. Alldredge, Quantification of marine snow fragmentation by swimming euphausiids. *Limnol. Oceanogr.* **49**, 940–952 (2004). doi:10.4319/lo.2004.49.4.0940

18. L. Dilling, A. L. Alldredge, Fragmentation of marine snow by swimming macrozooplankton : A new process impacting carbon cycling in the sea. *Deep Sea Res. Part I Oceanogr. Res. Pap.* **47**, 1227–1245 (2000). doi:10.1016/S0967-0637(99)00105-3

19. G. A. Jackson, Comparing Observed Changes in Particle-Size Spectra with Those Predicted Using Coagulation Theory. *Deep Sea Res. Part II Topical Stud. Oceanogr.* **42**, 159–184 (1995). doi:10.1016/0967-0645(95)00010-N

20. J. Ruiz, What generates daily cycles of marine snow? *Deep Sea Res. Part I Oceanogr. Res. Pap.* **44**, 1105–1126 (1997). doi:10.1016/S0967-0637(97)00012-5

21. N. Briggs, M. J. Perry, I. Cetinić, C. Lee, E. D'Asaro, A. M. Gray, E. Rehm, High-resolution observations of aggregate flux during a sub-polar North Atlantic spring bloom. *Deep Sea Res. Part I Oceanogr. Res. Pap.* **58**, 1031–1039 (2011). doi:10.1016/j.dsr.2011.07.007

22. R. A. Reynolds, D. Stramski, G. Neukermans, Optical backscattering by particles in Arctic seawater and relationships to particle mass concentration, size distribution, and bulk composition. *Limnol. Oceanogr.* **61**, 1869–1890 (2016). doi:10.1002/lno.10341

23. C. Roesler, J. Uitz, H. Claustre, E. Boss, X. Xing, E. Organelli, N. Briggs, A. Bricaud, C. Schmechtig, A. Poteau, F. D'Ortenzio, J. Ras, S. Drapeau, N. Haëntjens, M. Barbieux, Recommendations for obtaining unbiased chlorophyll estimates from in situ chlorophyll fluorometers: A global analysis of WET Labs ECO sensors. *Limnol. Oceanogr. Methods* **15**, 572–585 (2017). doi:10.1002/lom3.10185

24. See supplementary materials.

25. D. J. Mayor, R. Sanders, S. L. C. Giering, T. R. Anderson, Microbial gardening in the ocean's twilight zone: detritivorous metazoans benefit from fragmenting, rather than ingesting, sinking detritus. *BioEssays* **36**, 1132–1137 (2014). doi:10.1002/bies.201400100 Medline

26. N. Briggs, G. Dall'Olmo, H. Claustre, Size-fractionated optical backscattering and chlorophyll fluorescence from 34 high-latitude phytoplankton blooms. SEANOE (2019); https://doi.org/10.17882/70484.

27. X. Zhang, L. Hu, M. X. He, Scattering by pure seawater: Effect of salinity. *Opt. Express* **17**, 5698–5710 (2009). doi:10.1364/OE.17.005698 Medline

28. J. M. Sullivan, M. S. Twardowski, J. Ronald, V. Zaneveld, C. C. Moore, in *Light Scattering Reviews 7*, A. A. Kokhanovsky, Ed. (Springer, 2013), pp. 189–224.

29. N. T. Briggs, W. H. Slade, E. Boss, M. J. Perry, Method for estimating mean particle size from high-frequency fluctuations in beam attenuation or scattering measurements. *Appl. Opt.* **52**, 6710–6725 (2013). doi:10.1364/AO.52.006710 Medline

30. W. M. Berelson, The Flux of Particulate Organic Carbon Into the Ocean Interior: A Comparison of Four U.S. JGOFS Regional Studies. *Oceanography* **14**, 59–67 (2001). doi:10.5670/oceanog.2001.07

31. A. Waite, A. Fisher, P. A. Thompson, P. J. Harrison, Sinking rate versus cell volume relationships illuminate sinking rate control mechanisms in marine diatoms. *Mar. Ecol. Prog. Ser.* **157**, 97–108 (1997). doi:10.3354/meps157097

32. X. Y. Li, B. E. Logan, Size distributions and fractal properties of particles during a sumulated phytoplankton bloom in a mesocosm. *Deep Sea Res. Part II Topical Stud. Oceanogr.* **42**, 125–138 (1995). doi:10.1016/0967-0645(95)00008-E

33. A. Hatcher, P. Hill, J. Grant, Optical backscatter of marine flocs. *J. Sea Res.* **46**, 1–12 (2001). doi:10.1016/S1385-1101(01)00066-1

34. E. N. Flory, P. S. Hill, T. G. Milligan, J. Grant, The relationship between floc area and backscatter during a spring phytoplankton bloom. *Deep Sea Res. Part I Oceanogr. Res. Pap.* **51**, 213–223 (2004). doi:10.1016/j.dsr.2003.09.012